



HAL
open science

An all-solid-state laser source at 671 nm for cold atom experiments with lithium

Ulrich Eismann, Fabrice Gerbier, Carlota Canalias, Andrius Zukauskas, Gérard Tréneç, Jacques Vigué, Frédéric Chevy, Christophe Salomon

► **To cite this version:**

Ulrich Eismann, Fabrice Gerbier, Carlota Canalias, Andrius Zukauskas, Gérard Tréneç, et al. An all-solid-state laser source at 671 nm for cold atom experiments with lithium. 2011. hal-00580433v1

HAL Id: hal-00580433

<https://hal.science/hal-00580433v1>

Preprint submitted on 28 Mar 2011 (v1), last revised 28 Jun 2011 (v2)

HAL is a multi-disciplinary open access archive for the deposit and dissemination of scientific research documents, whether they are published or not. The documents may come from teaching and research institutions in France or abroad, or from public or private research centers.

L'archive ouverte pluridisciplinaire **HAL**, est destinée au dépôt et à la diffusion de documents scientifiques de niveau recherche, publiés ou non, émanant des établissements d'enseignement et de recherche français ou étrangers, des laboratoires publics ou privés.

An all-solid-state laser source at 671 nm for cold atom experiments with lithium

U. Eismann · F. Gerbier · C. Canalias · A. Zukauskas · G. Tréneç ·
J. Vigué · F. Chevy · C. Salomon

Received: date / Accepted: date

Abstract We present an all solid-state narrow line-width laser source emitting 670 mW output power at 671 nm delivered in a diffraction-limited beam. The source is based on a frequency-doubled diode-end-pumped ring laser operating on the ${}^4F_{3/2} \rightarrow {}^4I_{13/2}$ transition in Nd:YVO₄. By using periodically-poled potassium titanyl phosphate (ppKTP) in an external build-up cavity, doubling efficiencies of up to 86% are obtained. Tunability of the source over 100 GHz is accomplished. We demonstrate the suitability of this robust frequency-stabilized light source for laser cooling of lithium atoms. Finally a simplified design based on intra-cavity doubling is described and first results are presented.

Keywords Laser cooling of atoms · Lithium atoms · Diode-pumped solid state lasers · Frequency doubling

PACS 37.10.De · 42.55.Xi · 42.60.By · 42.60.Pk · 42.62.Fi · 42.65.Ky · 42.72.Ai · 42.72.Bj

U. Eismann · F. Gerbier · F. Chevy · C. Salomon
Laboratoire Kastler Brossel, ENS, UPMC, CNRS UMR 8552,
24 rue Lhomond, 75231 Paris, France
E-mail: eismann@ens.fr

G. Tréneç · J. Vigué
LCAR, Université de Toulouse, Université Paul Sabatier and
CNRS UMR 5589, F-31062 Toulouse, France

C. Canalias · A. Zukauskas
Department of Applied Physics, Royal Institute of Technology,
AlbaNova Universitetscentrum, SE-10691 Stockholm,
Sweden

1 Introduction

The lithium atomic species is of great interest for cold atom experiments and the study of quantum degenerate gases. As a member of the alkali group it offers strong coupling to electromagnetic fields and a simple level structure including cycling transitions, thus making it suitable for laser cooling. The significant natural abundance of fermionic (${}^6\text{Li}$) as well as bosonic (${}^7\text{Li}$) isotopes allows exploration of both sorts of quantum statistics. The interaction parameter at ultracold temperatures, the s-wave scattering length, is easily tunable for both species by applying a DC magnetic field in the vicinity of a Feshbach resonance [1]. The large width of these resonances, in addition to the light mass, adds up to the favourable properties of lithium for ultracold atom experiments.

To produce large samples of quantum degenerate gases, one needs large numbers of pre-laser-cooled atoms in a magneto-optical trap (MOT). This first step is mandatory before proceeding to the evaporative cooling phase that leads to quantum degeneracy by reducing the atom number in favor of phase-space density. To optimize the MOT capture process, one usually fixes the laser intensity around a saturation intensity and uses the available output power to maximize the beam diameter. Thus, more laser power leads to a better capture efficiency and larger atom numbers. Another important requirement is the quality of the spatial mode needed to efficiently couple the laser light to single mode (SM) optical fibers.

The wavelength of the lithium D-line resonances (670.8 nm in air) currently restricts the choice of light sources to two different kinds of lasers: dye lasers and external cavity diode lasers (ECDLs). Dye lasers typically deliver watt-level output of monochromatic light

in a diffraction limited beam [2]. The drawbacks of this technology are an important maintenance effort, high intrinsic phase noise, and the requirement of an expensive pump laser. ECDLs are typically limited to 50 mW output with limited spatial mode quality, hence further amplification by injection-locked slave lasers or tapered amplifiers is needed to run a cold-atom experiment.

It is thus desirable to develop suitable single-frequency lasers with watt-level output power. Further applications of such sources include atom interferometry experiments [3], pumping of Cr:LiSAF lasers [4] and lithium isotope separation [5].

Light sources emitting at 671 nm based on frequency-doubling of 1342 nm Nd:YVO₄ or Nd:GdVO₄ lasers have been realized previously [6–15], reaching up to 9.5 W of cw multi-mode output [15]. A solid state single-frequency laser source delivering 920 mW at around 657 nm has been presented in [16].

Here we report on the construction and characterization of an all-solid-state laser source with 670 mW output power in a TEM₀₀ mode operating at 671 nm. This is made possible by frequency doubling a home-made 1.3 W Nd:YVO₄ 1342 nm single mode ring laser in an external cavity. The advantages of our source are: watt-level output power in a single longitudinal and transverse mode with excellent beam quality, narrow linewidth (< 1 MHz), and long-term frequency stabilization onto the lithium resonance lines. Furthermore, multi-mode diode laser pumping at 808 nm is inexpensive and only low-maintenance efforts are required for establishing reliable day-to-day operation.

The paper is organized as follows: in Section 2 we describe the infrared single-frequency laser design and results. Section 3 focuses on the frequency doubling of the infrared radiation, whereas Section 4 treats the spectroscopy and frequency-locking systems. In Section 5 the red laser emission is characterized in terms of relative intensity noise, linewidth and longterm stability. In Section 6 we describe a second setup in progress using intra-cavity doubling that has the potential to deliver similar output power at 671 nm while offering higher simplicity of the laser source design.

2 Infrared laser

2.1 Laser setup

To realize a single-longitudinal-mode (SLM) laser it is favorable to use a design avoiding standing waves and thus the resulting spatial hole-burning in the active medium [17]. Thus we have chosen a ring cavity with proper intra-cavity etalons as frequency-selective elements.

The setup is presented in Fig. 1. The pump source is a commercial fiber-coupled Coherent FAP-400 diode stack emitting up to 42.6 W at 808 nm (90% energy width: 4 nm). Its metal housing is temperature stabilized to optimize the spectral overlap between pump emission and the gain medium absorption. The fiber output (core radius: 200 μm, numerical aperture $NA = 0.22$) is imaged in the gain medium using two lenses ($f_1 = 75$ mm and $f_2 = 200$ mm) to a top-hat spot of radius $w_{\text{pump}} = 530$ μm. The Nd:YVO₄ crystal of dimensions $3 \times 3 \times 10$ mm³ is 0.2 at.-%-doped, a-cut and anti-reflective (AR) coated at 808 nm and 1342 nm. It is wrapped in indium foil and fixed in a solid water-cooled copper mount to efficiently remove heat. Care needs to be taken to avoid acoustic excitations of the mount due to turbulent water flow, thus only a small continuous flux of tap water was applied to prevent frequency fluctuations of the laser output.

The four mirrors M_{1–4} (highly reflective at 1342 nm except the output coupler M₂, transmitting at 808 nm) form a folded ring or bow-tie cavity. The two concave mirrors M₃ and M₄ have a radius of curvature of $R_{cc} = 100$ mm. Thermal design is crucial for the laser: even at moderate pump powers, strong thermal lensing occurs because of the large quantum defect between pump and lasing photon energies and excited state absorption to higher levels [18, 19]. Optimum spatial overlap of the pump fiber image in the laser crystal (top-hat profile of radius w_{pump}) and laser mode ($1/e^2$ radius w_{laser}) is established by fine-tuning the distance between M₃ and M₄. The choice of the mode-size ratio $\rho = w_{\text{laser}}/w_{\text{pump}} \simeq 1$ allowed for a stable TEM₀₀ operation at optimum output power¹. The cavity design remains stable in presence of a thermal focal length down to $f_{\text{th}} = 170$ mm in the Nd:YVO₄ crystal. Care was taken to design the cavity as short as possible to increase the laser’s mechanical stability and the cavity free spectral range (FSR), facilitating SLM behavior.

Unidirectional oscillation is ensured by a combination of a Faraday rotator and a wave plate. The Faraday rotator is custom built by the LCAR group according to the original design presented in [21]. As a medium displaying the Faraday effect, a cylindrical AR-coated Terbium Gallium Garnet (TGG) crystal is chosen. To minimize absorption, the length of the TGG crystal is limited to $l_{\text{TGG}} = 6$ mm, and its diameter is 5 mm. The ensemble of NdFeB ring magnets delivers a magnetic field integral of $I_B = \int_0^{l_{\text{TGG}}} B(z) dz = 8$ T.mm along the TGG axis. Single-pass measurements resulted in a rotation angle of $\varphi_{\text{rot}} = -(9.3 \pm 0.1)^\circ$ and thus in a Verdet

¹ Ref. [20] suggests a ratio $\rho = 0.8$ for which we observe reduced output power as well as higher-order transversal mode oscillation.

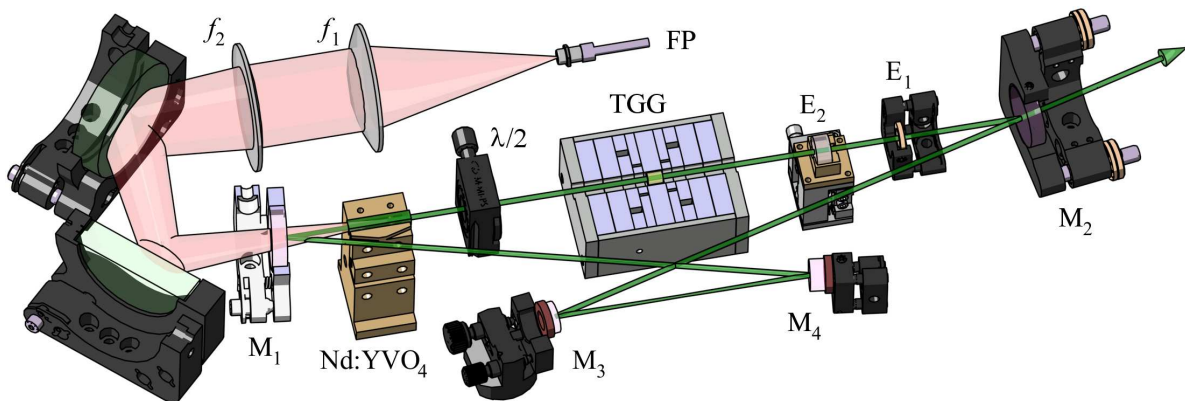


Fig. 1 (Color online) The laser setup, consisting of the fiber coupled pump source FP, two pump focusing lenses $f_{1,2}$, the cavity mirrors M_{1-4} and the Nd:YVO₄ active medium. The $\lambda/2$ wave plate and the TGG Faraday crystal in a magnet ensemble impose unidirectional oscillation whereas two etalons $E_{1,2}$ establish single-mode operation. The optical path of the laser beam is depicted in green. For some mechanical components we show a sectional view to improve visibility of the beam path. The distance between M_1 and M_2 is 295 mm.

Table 1 Frequency scales in the setup. Typical frequencies are free spectral ranges ν_{FSR} as described in the text and FWHM for the gain profile from [18]. Reflectivities \mathcal{R} are given for the output and input coupling mirrors in case of the two cavities and for the two etalon surfaces, respectively. The finesses \mathcal{F} and Q-factors of the laser cavity and E_1 are calculated from the \mathcal{R} -values as stated, neglecting further losses. \mathcal{F} and Q were measured for the doubling cavity, see Section 3.3.

	Typ. freq.	Typ. \mathcal{R}	$\mathcal{F}/\text{Q-factor}$
Gain profile width	300 GHz		
Laser cavity 81 cm	360 MHz	96.5%	110 / 6×10^7
Doub. cavity 41 cm	730 MHz	93.6%	86 / 3×10^7
Etalon E_1 , 0.5 mm	210 GHz	3.3%	-/-
Etalon E_2 , 4 mm	26 GHz	28%	2 / 2000

constant of $\mathcal{V} = \varphi_{\text{rot}}/I_B = -(20.3 \pm 0.2) \text{ rad} \cdot \text{T}^{-1} \cdot \text{m}^{-1}$ for the given crystal at 1342 nm. Back rotation and stable unidirectional operation at high intra-cavity powers is established by an AR-coated zero-order $\lambda/2$ -wave plate, which is preferred to multi-order wave plates because of instabilities related to thermal effects [22]. The polarizing intra-cavity element is the Nd:YVO₄ crystal which provides higher gain in the c-direction as well as birefringence. The oscillation direction is chosen as indicated in Fig. 1 to spatially separate residual pump light from the output beam.

Stable SLM behavior could not be established using a single intra-cavity etalon. Thus, two infrared fused silica etalons $E_{1,2}$ of free spectral range $\nu_{\text{FSR},1} = 210 \text{ GHz}$ and $\nu_{\text{FSR},2} = 26 \text{ GHz}$ are installed, where $\nu_{\text{FSR}} = c/nL_{\text{rt}}$, c is the speed of light in vacuum, n the refractive index and L_{rt} the round-trip length. An overview of the typical frequency scales of the setup is given in Table 1. E_1 is non-coated, offering a modulation of the cavity transmission due to its Fresnel reflectivity of $\mathcal{R} = 3.3\%$

per surface, whereas E_2 is single-layer coated, yielding $\mathcal{R} = 28\%$.

A second role of the etalons is coarse frequency tuning of the output radiation. However, angular tuning yields walk-off losses and thus reduces the available output power. By applying the method of [23] to ring lasers, the minimum walk-off loss² can be estimated to $\mathcal{L}_{\text{wo}} = 0.02\%$ for E_2 . It can be neglected for E_1 , for which even an angular tuning of an entire free spectral range only yields $\mathcal{L}_{\text{wo}} = 0.03\%$ additional loss. To avoid the higher tilt loss of E_2 ($\mathcal{L}_{\text{wo}} = 2.8\%$ for angular tuning over one free spectral range of $\nu_{\text{FSR}} = 26 \text{ GHz}$), we chose to keep it still at the minimum angle and to change its temperature to tune the laser. For that purpose, it is enclosed in a temperature-stabilized copper mount.

Fine tuning of the laser frequency is established by mounting mirrors M_3 and M_4 on piezoelectric transducers (PZTs): a slow PZT (M_4) displaying large displacement of around $2 \mu\text{m}$ at maximum voltage of 150 V and a fast PZT (M_3) with a displacement of around $\pm 50 \text{ nm}$ limited by the $\pm 15 \text{ V}$ driver.

The laser was mounted on a 50 mm-thick breadboard. A combined aluminum-acrylic-glass housing was provided to isolate from acoustic perturbations and for keeping the setup continuously under a dried air atmosphere to prevent dust and moisture from having detrimental effects on stable long-term operation.

² The loss estimate of ref. [23] yields zero for perpendicular incidence. However, one needs to account for a minimum angle on the order of the Gaussian beam divergence angle to circumvent multi-cavity behavior, causing instability of laser operation.

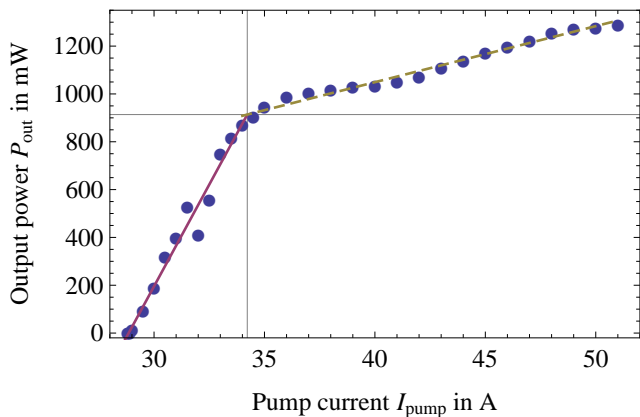


Fig. 2 (Color online) Single-frequency laser output power as a function of pump current. Two regimes can be distinguished in the data (circles), and linear fits are performed (solid/dashed line).

2.2 Laser operation and characteristics

We now present a detailed description of the laser’s operational characteristics. Pump light absorption in the gain medium depends on the wavelength of the radiation [24], hence on the pump diode stack temperature. Setting the chiller temperature to 24°C at maximum pump current resulted in highest output power.

By choosing a coupling mirror transmission value $T_{oc} = 3.5\%$, a maximum single-mode output power P_{out} of 1.3 W was obtained, see Fig. 2. The lasing threshold was found at a pump current $I_p = 28.8$ A. The power rises linearly above threshold with a slope of $\eta_{sl} = dP_{out}/dI_p = 170$ mW/A. At $I_p(P_{out}) = 34.2$ A (910 mW) the slope suddenly drops to $\eta_{sl} = 23$ mW/A, indicating the presence of detrimental thermal effects. This behavior was qualitatively found before, see for instance ref. [25]. Since no degradation of the laser parameters was observed for highest output powers, the laser was always pumped at maximum current for all further measurements. Removal of the etalons yields a rise in output power of $\sim 20\%$. This can be partly attributed to detuning of the laser frequency ω of $\simeq 25$ GHz from the emission peak when lasing at half the lithium resonance frequency.

The temperature derivative of the frequency of maximum etalon transmission ν_{max} yields

$$\frac{d\nu_{max}}{dT} = \frac{\nu_{max}}{\nu_{FSR}} \frac{d\nu_{FSR}}{dT} = -\nu_{max} \left(\frac{1}{n} \frac{dn}{dT} + \frac{1}{L_r} \frac{dL_r}{dT} \right), \quad (1)$$

where T is the etalon temperature. Putting in the values for IR fused silica from [26] yields $d\nu_{max}/dT = -1.42$ GHz.K⁻¹. The emission wavelength was measured by single-pass frequency doubling the laser light, as described in the next section. This resulted in a second-harmonic (SH) output power in the 1-mW

range, sufficient to drive a CCD-based wavelength meter (High Finesse WS-6). The measured temperature dependence of the laser emission frequency ν is $d\nu/dT = (-1.45 \pm 0.01)$ GHz.K⁻¹. Tunability of $\simeq 50$ GHz is achieved, yielding $\simeq 100$ GHz of tunability for the SH output. To operate the laser at a given frequency without mode hops caused by etalon temperature drifts, the temperature of the etalon T_{set} needs to be stabilized to an interval $T_{set} \pm \delta T$, where δT can be estimated to

$$\delta T < \frac{\nu_{FSR, laser}}{2 |d\nu/dT|} \simeq 0.1^\circ\text{C}. \quad (2)$$

This is accomplished using a homemade temperature controller, offering stability well below this requirement.

Continuous scanning of the laser frequency is achieved by sweeping the voltage applied to the slow PZT (M_4). For the dynamic range of 0...150 V this results in more than three times the full mode-hop-free scan range of $\nu_{FSR, laser} = 360$ MHz. By applying simultaneous (linear) scanning of the PZT and angle-tuning of etalon E_2 , mode-hop free continuous frequency tuning of the laser over 1.1 GHz could be demonstrated, with a resulting maximum output power drop of $\simeq 10\%$ due to etalon walk-off loss.

The beam coupled out of M_2 has a $1/e^2$ waist radius of 640 μm (820 μm) and a divergence angle of 0.8 mrad (0.9 mrad) in the horizontal (vertical) plane. The astigmatism results from the cavity design and non-isotropic thermal lensing in the Nd:YVO₄ crystal. By employing only spherical lenses, and thus imperfect mode matching, a coupling efficiency to a SM optical fiber of 75% was obtained. Stable output power and beam parameters over weeks of daily operation were demonstrated.

3 Second-harmonic generation

3.1 General considerations

Frequency-doubled light is generated using a second order process in a nonlinear medium. In the limit of weak conversion this yields a second harmonic (SH) output power $P_{2\omega}$ in the form

$$P_{2\omega} = \eta P_\omega^2, \quad (3)$$

with P_ω the pump beam power of frequency ω and η the conversion efficiency. In [27], Boyd and Kleinman derived the following expression for η , assuming Gaussian beams:

$$\eta = \frac{2\omega^3 d_{ij}^2 L}{\pi \epsilon_0 c^4 n_{\omega, i} n_{2\omega, j}} h(\alpha, \beta), \quad (4)$$

where d_{ij} is the effective nonlinear coefficient of the material with $i(j)$ the polarization of the fundamental

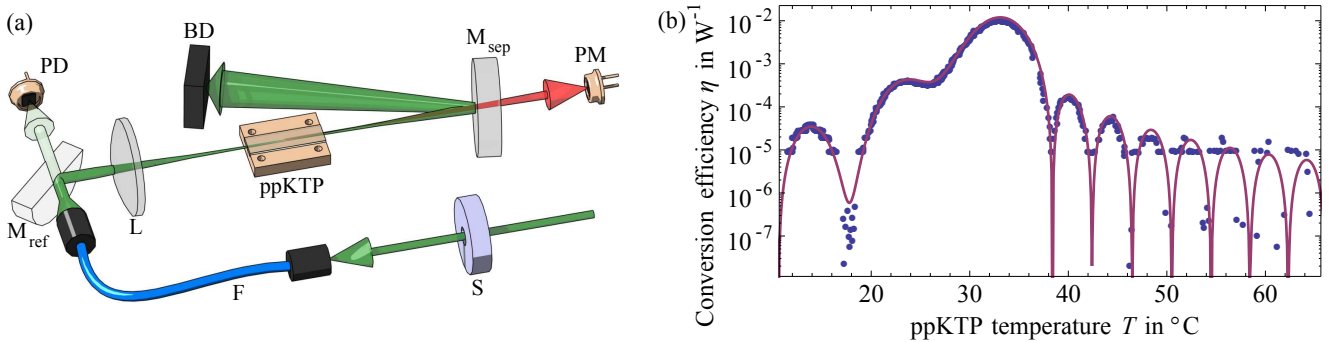


Fig. 3 (Color online) (a) Setup of the single pass efficiency measurements. The IR laser output (depicted in green) is mode-cleaned by a polarization-maintaining SM fiber (F). The power leaking through mirror M_{ref} is referenced on a photodiode (PD), and the beam is then focused into the ppKTP crystal by a lens (L). Mirror M_{sep} separates SH (red) from fundamental light, which is sent in a beam dump (BD), whereas the converted light power is measured with a power meter (PM). For referencing to the dark-current values, a shutter periodically switches on and off the IR light. (b) Temperature-dependent single-pass doubling efficiency. Measured data (circles), fit to eq. (5) (solid line).

(SH) wave, $n_{\omega(2\omega),i(j)}$ the corresponding refractive indices of the material, L the nonlinear material length, ϵ_0 the vacuum permittivity and c the speed of light in vacuum. The function $h(\alpha, \beta)$ is given as

$$h(\alpha, \beta) = \frac{1}{4\alpha} \left| \int_{-\alpha}^{\alpha} \frac{e^{i\beta(T)\tau}}{1+i\tau} d\tau \right|^2, \quad (5)$$

with the focusing parameter $\alpha = L/2z_R$, where z_R is the Gaussian beam Rayleigh length assumed here equal for both waves, yielding a smaller waist for the SH light. The phase-matching parameter

$$\beta = \frac{4\pi z_R}{\lambda} (n_{\omega,i}(T) - n_{2\omega,j}(T)) \quad (6)$$

is temperature- and polarization-dependent in the case of birefringent media. The derivation assumes no depletion of the fundamental wave and absence of losses. The integral in eq. (5) needs to be calculated numerically except for limiting cases, yielding a global maximum of $h_{\text{max}}(2.84, 0.573) = 1.068$. Putting in values for the usual nonlinear media, this results in a doubling efficiency η in the %/W range at best. Thus for the available cw laser power, single pass doubling is not an option and one has to resort to resonantly enhanced intracavity doubling.

Quasi-phase matching in periodically-poled materials is favorable in the intracavity case because of the excellent beam quality achievable without beam walk-off [28, 29]. The accessibility of the much greater diagonal elements d_{ii} of the nonlinear tensor allows for higher single-pass efficiencies (eq. (4)) while keeping the phase matching condition of optimum β . Compared to the bulk case, the same equations (3)-(6) hold, by performing the following replacements: $\beta \rightarrow \beta - 2\pi z_R/\Lambda$ where Λ is the poling period and $d_{ij} \rightarrow d_{\text{eff}} = 2d_{ii}/\pi$. As a nonlinear medium, periodically-poled Potassium

Titanyl Phosphate (ppKTP) was chosen because of its high transparency from 350-4300 nm, its high nonlinear coefficient $d_{33} = 16.9$ pm/V [30] and its high damage threshold.

3.2 Single pass measurements

We first describe the characterization of the nonlinear crystal using a single-pass method. The completely automated measurement setup is represented in Fig. 3. The spatial mode-cleaning fiber output power was $\simeq 500$ mW, resulting in a maximum of $P_{2\omega} \simeq 2$ mW of red light output, the two beams being separated using mirror M_{sep} . The fundamental power was monitored using a Ge photodiode (PD) exploiting the finite transmission through mirror M_{ref} . The signal was calibrated against the IR power P_{ω} hitting the crystal. The finite transmittance of M_{ref} at 671 nm was taken care of, and the SH power measured using a commercial power meter (Thorlabs S130A). The response of the power meter's Si photodiode at 1342 nm is negligible, and so is the corresponding transmission of M_{sep} . The shutter, driven at 1 Hz with a 50% duty cycle allowed for the determination of dark current offset drifts for both power measurements, which is of highest importance for low conversion efficiencies. The crystal is mounted on a transverse (xy -) translation stage and temperature controlled to ~ 10 mK using a Peltier element and a homemade temperature controller. A set temperature ramp was applied to the controller, scanning the full 55°C range in about 30 minutes. The slow ramp allowed for adiabatic behavior of the temperature measurement, permitting independent determination of the temperature of the crystal measured by a LM35 sensor attached to the crystal mount.

The ppKTP crystal used in the experiments was fabricated in-house at the Royal Institute of Technology by electric field poling at room temperature [31]. Its length is 19.2 mm, featuring an optical aperture of $6 \times 1 \text{ mm}^2$. The length of the periodically-poled region is 17.25 mm. The poling period was chosen to be $\Lambda = 17.61 \mu\text{m}$, resulting in expected plane-wave phase matching at 23.5°C using the temperature-dependent Sellmeier equations from [32, 33]. Both surfaces are AR coated at 1342 nm and 671 nm.

Experimental results are presented in Fig. 3. A weighted numerical fit to the eq. (4) well describes the measured data. The temperature dependence of the phase matching parameter β was taken into account up to quadratic order. The full 99%-width of the peak of 0.7°C allows the use of standard temperature controllers. However, the optimum phase-matching temperature of 33.2°C differs from the theoretical value. This can be explained by a small difference to the Sellmeier equations as presented in [33] and a non-perfect alignment between pump beam and crystal axis. The maximum measured single pass efficiency of $1.13\%/W$ represents 74% of the theoretical maximum of $1.53\%/W$ from formula (4) with the parameters α as fitted and d_{33} for KTP from [30]. This can be explained by imperfections of the domain grating, most probably deviations from the 50% duty cycle. We thus derive an effective nonlinear coefficient of $d_{\text{eff}} = 9.2 \text{ pm/V}$ for our crystal.

3.3 Doubling cavity

The doubling cavity setup is similar to the one presented in [34] and depicted in Fig. 4. As for the laser, a four-mirror folded ring-cavity is used, building up a powerful traveling fundamental wave. The pump light is coupled through the plane mirror M'_1 for which several reflectivity values \mathcal{R}_c are available to account for impedance matching. All other mirrors are highly reflective at 1342 nm and transmitting at 671 nm. M'_3 and M'_4 are concave with a radius of curvature of 75 mm. M'_2 (M'_3) was glued on the same type of fast (slow) PZT as used in the laser cavity (Section 2.1), allowing to act on the cavity length in the 50 nm ($2 \mu\text{m}$) range. The nonlinear crystal is inserted in the cavity's smaller waist of $w_0 \simeq 55 \mu\text{m}$. The weaker-than-optimal focusing leads to a slightly reduced $h(\alpha = 1.22, 0.818) = 0.865$, or a fraction $h/h_{\text{max}} = 81\%$ of the optimum value, yielding $\eta = 0.92\%/W$. This choice represents a trade-off between maximum single-pass doubling efficiency and intensity-related detrimental effects such as nonlinear and SH-induced absorption [35] and gray-tracking [36]. The cavity length was minimized and the geometry chosen to be shifted with respect to the stability range cen-

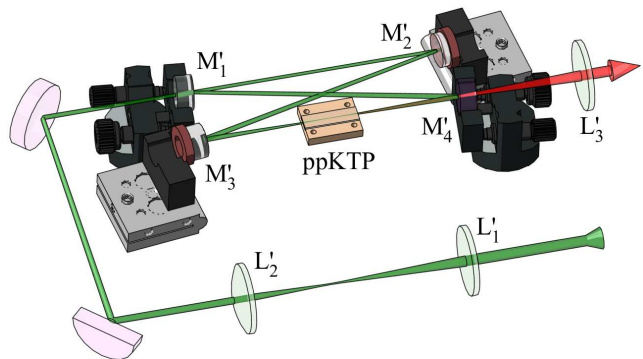


Fig. 4 (Color online) The doubling cavity setup consisting of the four mirrors M'_{1-4} and the ppKTP nonlinear crystal. The light is coupled to the cavity eigenmode using lenses $L'_{1,2}$, whereas L'_3 collimates the SH output. Some mechanical components are sectioned to improve visibility of the laser (SH) beam, depicted in green (red). The distance M'_3 – M'_4 is 95 mm, the dimensions of the coupling light paths are not to scale.

ter. It also avoids frequency degeneracy of higher-order transverse cavity eigenmodes and the TEM_{00} mode. It also accounts for a circular beam in the crystal and thus for a circular SH output. Mode matching between the laser output and the cavity was accomplished using a set of spherical lenses. The crystal mount is identical to the one described in Sect. 3.2. The frequency doubled light is transmitted through M'_4 and collimated using a $f'_3 = 150 \text{ mm}$ lens to a $1/e^2$ beam radius of 0.9 mm. The doubling cavity is kept in a housing equaling the laser housing in design and function.

For low intra-cavity powers of up to $\sim 500 \text{ mW}$ and the crystal temperature tuned far from the optimum phase matching value, nonlinear conversion can be neglected. While scanning the cavity length by ΔL , one measures a power signal leaking through M'_2 , proportional to the intra-cavity power

$$P(\delta L) = \sum_{lm} \frac{P_{lm}}{1 + F \sin^2(\varphi_{lm} + \omega \Delta L/c)}, \quad (7)$$

where F is a fit parameter. P_{lm} are the contributions from the TEM_{lm} modes, displaying a constant cavity round-trip phase of φ_{lm} , and c is the speed of light in vacuum. The mode matching efficiency is defined as $\eta_{\text{mo}} = P_{00}/\sum P_{lm}$. It was maximized to $\eta_{\text{mo}} = 92\%$. The linear cavity round-trip losses $\mathcal{L}_{\text{emp/tot}}$ can be quantified from the fit parameter F , where emp(tot) means the empty cavity (cavity including ppKTP crystal). The results are presented in Table 2. Inserting the crystal rises the losses by $\mathcal{L}_c \simeq 1\%$. This can be accounted for by residual absorption and scattering in the ppKTP crystal and imperfections of its AR coatings. Taking into account nonlinear conversion, the fundamental mode intracavity power $P_{00} = P_\omega$ at TEM_{00}

Table 2 Passive losses in the doubling cavity measured from cavity transmission spectra at low power and conversion efficiency. $(1 - \mathcal{R}_c)$ is the specified coupler power transmission, \mathcal{L}_{emp} are the measured empty-cavity round trip power losses, \mathcal{L}_{tot} are losses including the ppKTP crystal, and \mathcal{L}_c are the inferred crystal insertion losses according to $\mathcal{L}_c = 1 - (1 - \mathcal{L}_{\text{tot}}) / (1 - \mathcal{L}_{\text{emp}})$.

$1 - \mathcal{R}_c$	\mathcal{L}_{emp}	\mathcal{L}_{tot}	\mathcal{L}_c
5%	6.4%	7.1%	0.7%
10%	10.4%	11.2%	0.9%
17%	17.9%	19.0%	1.3%

resonance (referred to as cavity resonance) is a solution of

$$P_\omega = \frac{(1 - \mathcal{R}_c - \mathcal{L}_1)\eta_c P_p}{\left(1 - \sqrt{\mathcal{R}_c(1 - \mathcal{L}_{\text{pa}})(1 - \eta P_\omega)}\right)^2}, \quad (8)$$

which can be calculated numerically, where P_p is the fundamental pump power, \mathcal{L}_1 is the coupling mirror (M'_1) transmission loss and \mathcal{L}_{pa} is the total cavity passive loss excluding the coupler transmission. The single-pass doubling efficiency η is calculated according to eq. (4) with d_{33} as measured in Section 3.2. Setting $\mathcal{L}_{\text{pa}} = \mathcal{L}_c$ and $\mathcal{L}_1 = 0$ the solution of eq. (8) yields a maximum SH power of 710 mW at the maximum available pump power of $P_p = 860$ mW. This is accomplished for an optimized coupling mirror reflectivity of $\mathcal{R}_c = 92\%$, yielding a power conversion efficiency of $\eta_{\text{conv}} = P_{2\omega}/P_p = 84\%$.

After locking the cavity to the laser, as will be described in Section 4.1, the SH power $P_{2\omega}$ versus P_ω was measured for $\mathcal{R}_c = 95\%$, see Fig. 5. For low powers, the conversion shows quadratic behavior as stated in eq. (3). A fit yields a single-pass efficiency of $\eta = 0.78\%/W$, slightly lower than predicted. However, starting from the threshold value $P_\omega(P_{2\omega}) = 9.0$ W (640 mW), only a slow linear rise in SH power with intra-cavity power is obtained, reaching its maximum at $P_\omega(P_{2\omega}) = 10.7$ W (670 mW). We attribute this behavior to fast intensity-dependent detrimental effects. This is confirmed by the lock error signal, which becomes very noisy above threshold. In contrast to [37, 38] the cavity remains locked for all power levels. When changing the pump power, the SH output follows without observable hysteresis. Long-term degradation is not observed, indicating the absence of gray-tracking. However, for further characterization the setup is operated just below threshold to avoid the related rise in intensity noise. A maximum doubling efficiency of $\eta_{\text{conv}} = 86\%$ is obtained just below threshold, compatible with the theoretical predictions.

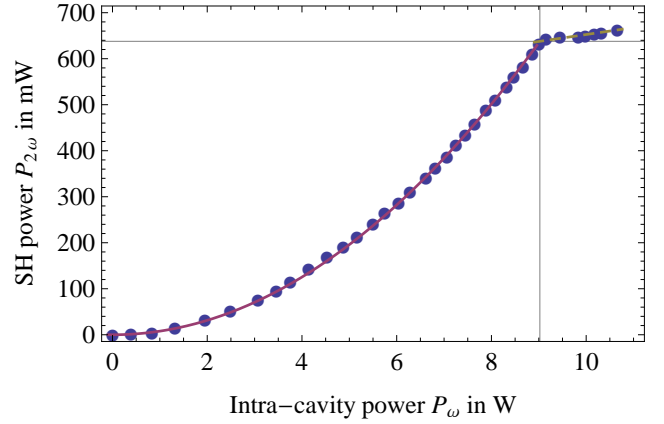


Fig. 5 (Color online) Intra-cavity conversion for the cavity locked to the laser, as described in Section 4.1. Measured data (circles) versus parabolic fit (solid line). At $P_{2\omega} = 640$ mW the conversion becomes less efficient (dashed line).

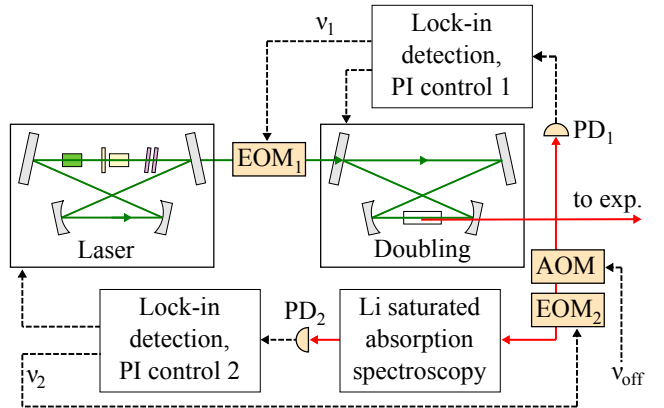


Fig. 6 (Color online) Locking scheme. Straight lines depict light paths, dashed lines electronic signals. First the doubling cavity is locked to the free-running laser using control circuit components indexed 1. A part of the SH light is used for lithium spectroscopy. In a second step this reference serves to lock the laser frequency with respect to half of one of the lithium resonance frequencies with a tunable offset, using control circuit 2. The frequency offset is determined by the double pass AOM driving frequency ν_{off} .

4 Lock and saturation spectroscopy

Frequency locking of the laser system to the lithium D-line transitions requires frequency doubled light to perform spectroscopy on atomic lithium vapor. Thus, first the doubling cavity needs to be frequency-locked to the free-running laser. In a second step, the laser is stabilized to half the required frequency using lithium saturated absorption phase modulation spectroscopy. The setup is presented in Fig. 6.

4.1 Cavity lock

To frequency-lock the doubling cavity to the laser frequency, an error signal needs to be generated. We use a modulation technique: An electro-optical modulator (EOM₁ in Fig. 6) phase-modulates the infrared pump light at a modulation frequency of $\nu_1 = 1$ MHz. In the doubling process, this results in a phase modulation of the frequency-doubled light, which is detected and demodulated using a homemade synchronous detection circuit. It allows to produce an error signal with a 3 dB-bandwidth of 100 kHz, which is fed into a lock circuit.

The lock circuit combines a proportional-integrating (PI) stage and splits the resulting lock signal in two frequency ranges: 0 Hz to $\nu_{3\text{ dB,slow}} = 72$ Hz for the slow PZT and 72 Hz to $\nu_{3\text{ dB,fast}} = 34$ kHz. The amplitude of the slow PZT signal is further amplified by a commercial high-voltage amplifier (Falco Systems WMA-280). The upper frequency limits were chosen to avoid oscillation of the loop at resonances attributable to the PZTs. When scanning the laser frequency via the slow PZT (M₄), the ramp signal (modified by an adjustable gain) is fed-forward to the lock signal, thus minimizing lock deviations and stabilizing output power. The implementation of the re-locking scheme of ref. [39] renders the doubling cavity lock significantly more stable to external disturbances.

4.2 Saturation spectroscopy and laser lock

A small fraction of the frequency-doubled light is sent through a 200 MHz acousto-optic modulator (AOM) double-pass setup to frequency-shift the light used for spectroscopy by $2\nu_{\text{mod}}$. It is employed to perform saturated absorption spectroscopy in an atomic lithium vapor cell. The required vapor pressure is obtained by heating a metallic lithium sample of natural isotope composition (8% ⁶Li, 92% ⁷Li) up to 330°C under vacuum. We use a 50 cm long CF-40 tube with broadband AR-coated windows. The final sections of the tube are water-cooled to prevent from too high temperatures at the CF-40 flanges and windows. Nickel gaskets are employed because of their chemical inertness to lithium vapor. A small amount of argon buffer gas is used to force lithium atoms by collision to stick to the side walls before arriving at the window surfaces. The argon pressure is kept low enough to not cause significant collisional broadening of the saturated spectroscopy lines. A metallic mesh put inside the tube covers the tube walls to regain condensed lithium from the colder parts exploiting the temperature-dependent surface tension.

The spectroscopy beam $1/e^2$ -radius is $\simeq 1$ mm, the pump power is of the order of 10 mW, of which typi-

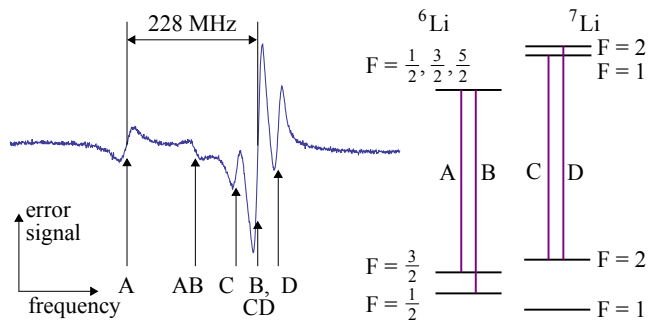


Fig. 7 (Color online) (a) Lock-in saturated absorption spectroscopy of lithium vapor, and corresponding transitions (b). The transitions are $2^2S_{1/2} \rightarrow 2^2P_{3/2}$ for ⁶Li (D2) and $2^2S_{1/2} \rightarrow 2^2P_{1/2}$ for ⁷Li (D1). Not all levels are shown, and the hyperfine structure of the ⁶Li excited state remains unresolved. Double indexes mark crossover lines.

cally 50% are transmitted through the lithium cell on atomic resonance. The beam then passes through a ND filter and an EOM₂, which serves to phase-modulate the light at $\nu_2 = 20$ MHz. A quarter-wave plate and a mirror retro-reflect the beam with a polarization rotated by 90°, thus creating the probe beam of ~ 200 μ W power. Around 100 μ W of probe light are detected on a fast photodiode (Newport 1801). Lock-in detection using a commercial amplifier (Toptica PD110) allows to generate a dispersive error signal. A typical example of a $\simeq 600$ MHz-scan over a part of the lithium lines is shown in Fig. 7. The hyperfine structure of both lithium isotopes is clearly resolved and error signals of $\text{SNR} \geq 100$ in a 1-MHz bandwidth are detected. The saturated spectroscopy transmission signal can serve as the auto re-lock reference. This requires a well pronounced peak or dip structure as satisfied for some of the lines.

To lock the laser frequency with respect to one of the resonances, a two-way PI circuit similar to the one used for locking of the doubling cavity is employed. The AOM frequency and thus the lock offset frequency can be changed by a few MHz while the laser remains locked.

5 Laser characterization

We now present further characterizations of the light source in terms of intensity noise and linewidth. The excellent beam quality of the SH light is confirmed by a SM fiber coupling efficiency of 83%.

5.1 Relative intensity noise

The relative intensity noise spectral density $S_{\text{RIN}}(\nu)$ of the SH output was measured by shining a beam of

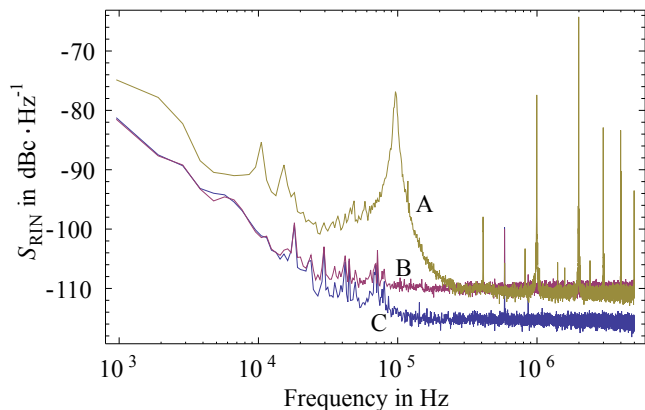


Fig. 8 (Color online) The SH relative intensity noise spectrum (A), noise for an equivalent photocurrent from a non-coherent source (B) and noise of the detection circuit with no photocurrent (C).

$\sim 120 \mu W$ on a low-noise photodiode (Newport 1801, 125-MHz bandwidth) and recording the signal using a digital oscilloscope (Pico Technology PicoScope 4424) in AC mode, yielding the relative power fluctuations $\varepsilon(t)$ after normalization, where $I(t)/\langle I \rangle_T = 1 + \varepsilon(t)$ with $I(t)$ the intensity and $\langle I \rangle_T$ its temporal average. The definition of $S_{\text{RIN}}(\nu)$ is

$$S_{\text{RIN}}(\nu) = \lim_{t_m \rightarrow \infty} \frac{1}{t_m} \left\langle \left| \int_0^{t_m} \varepsilon(t) e^{i2\pi\nu t} dt \right|^2 \right\rangle \quad (9)$$

with the measurement time t_m and $\langle \dots \rangle$ denoting temporal averaging. It was realized employing a time-discrete Fourier transformation method and averaging over 100 spectra.

The result is shown in Fig. 8. The broad peak at $\simeq 100$ kHz can be attributed to the laser relaxation oscillations. The structure in the 10 kHz region can be attributed to the locking system. Above 300 kHz S_{RIN} drops to the photon shot-noise level, as indicated by the spectrum of a noncoherent source producing an equivalent photocurrent (spectrum B in Fig. 8). The narrow peaks at 1 MHz and harmonics stem from the phase modulation of the pump light, see Section 4.1. The square root of the integral of $S_{\text{RIN}}(\nu)$ from 1 kHz to 5 MHz (1 kHz to 0.9 MHz) yields a RMS relative intensity noise of 1.1×10^{-3} (0.8×10^{-3}).

5.2 Absorption spectroscopy of ultracold atoms

The laser setup was used as an absorption imaging light source for our lithium quantum gas experiment described elsewhere [40]. A sample of around 1.2×10^5 ^7Li atoms above Bose-Einstein condensation threshold was prepared in an elongated optical dipole trap. Putting a 700 G magnetic offset field, the internal electronic states

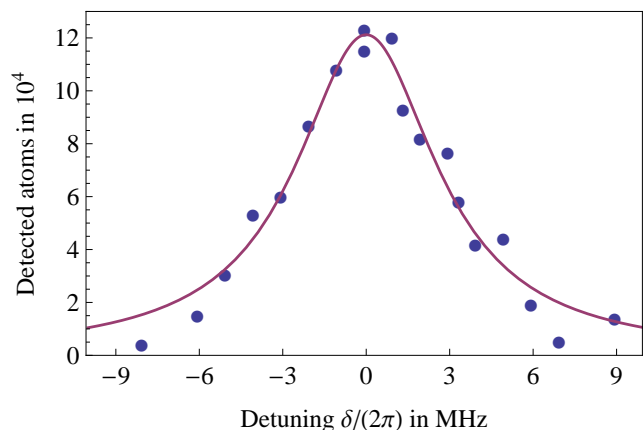


Fig. 9 (Color online) In-situ absorption imaging of ultracold atoms in an optical dipole trap. The laser was detuned by δ from the atomic resonance using the offset lock described in Section 4.2, varying the detected atom number (circles). A Lorentzian of width $\Gamma_{\text{fit}} = 2\pi \times (6.1 \pm 0.4)$ MHz is fitted to the data (solid line).

of the atoms are to be described in the Paschen-Back regime. The corresponding lift of degeneracy for the $F = 2 \rightarrow F' = 3$ transition frequencies results in a cycling transition, rendering this method insensitive to constant homogeneous stray fields. By applying a laser frequency detuning δ with respect to atomic resonance using the offset lock as described in section 4.2, one detects a different atom number $N(\delta)$ while assuming constant trap conditions according to

$$\frac{N(\delta)}{N(0)} = \left[1 + \left(\frac{2\delta}{\Gamma} \right)^2 \right]^{-1}, \quad (10)$$

where Γ is the measured linewidth of the transition and $N(0)$ the atom number detected at resonance. The results are presented in Fig. 9. A least-squares fit according to eq. (10) results in a linewidth of $\Gamma_{\text{fit}} = 2\pi \times (6.1 \pm 0.4)$ MHz, a value compatible with the natural linewidth of $2\pi \times (5.872 \pm 0.002)$ MHz of [41]. Within our experimental resolution we infer that the laser linewidth is much smaller than the natural linewidth of the atomic transition. Assuming a Lorentzian lineshape for the laser, the linewidth can be given as 200_{-200}^{+400} kHz, compatible with zero.

5.3 Long-term stability

Fig. 10 shows a long-term stability plot of the laser system under laboratory conditions. The system remained locked during the measurement time of 8.5 hours. The SH output power drops by 7% and shows small modulations of a period of $\simeq 15$ min. This is attributable to slight angular tilts when the cavity's slow PZT (M_4/M_3)

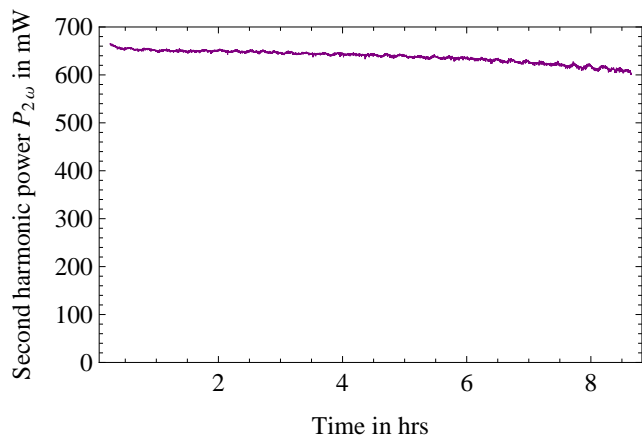


Fig. 10 (Color online) Long-term stability of the SH output power, experiencing a drop of 7% over the measurement time. The system remained offset-locked to the lithium resonance.

is driven. This effect, changing the alignments, is confirmed by monitoring the laser output power, which drops by 5% in the same time interval and displays the same modulations.

6 Intra-cavity doubling

We also implemented the more direct approach of intra-cavity doubling a 1342-nm laser. This concept simplifies the optical design since only one cavity is needed. It was achieved by using a setup similar to the one presented in Fig. 1. All cavity mirrors are highly reflective at 1342 nm and mirror M_3 is also transmitting at 671 nm. A nonlinear crystal is put in the waist between mirrors M_3 and M_4 .

For the Faraday rotator, we have tried various arrangements, using either Gadolinium Gallium Garnet (GGG) or TGG as the Faraday material and we have used either a rotatory power plate (made either of TeO_2 or of crystalline quartz) or a half-wave plate to compensate the Faraday rotation. Although theory [42] favors the use of a rotatory power with respect to a half-wave plate, we have found that the wave plate was more convenient, with a slightly larger output power.

6.1 Infrared power

In a setup involving intra-cavity frequency doubling, it is essential to have very low parasitic losses \mathcal{L}_{par} [43]. We start by evaluating these losses by measuring the emitted infrared laser power as a function of the output mirror transmission \mathcal{T}_{oc} for a fixed absorbed pump power $P_{\text{abs}} = 13 \text{ W}$ for which thermal effects in the Nd:YVO_4 crystal remain small. The data is presented

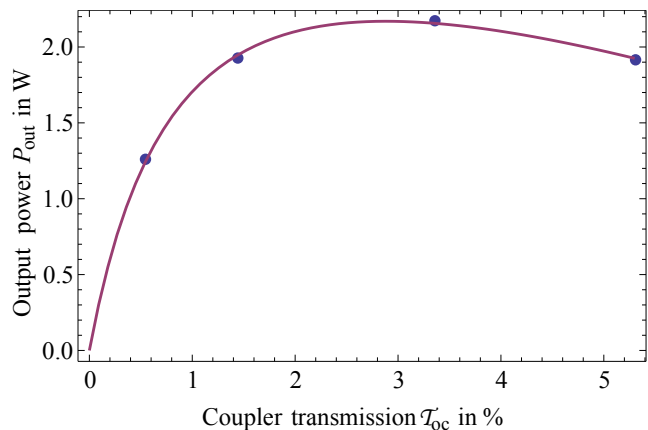


Fig. 11 Output power P_{out} of the laser emitting at 1342 nm as a function of the mirror transmission \mathcal{T}_{oc} . The data points are experimental while the curve is the best fit using eq. (11).

in Fig. 11. Accurate values of the transmission coefficient of the various output mirrors have been obtained with an absolute uncertainty near 0.03% by measuring successively the direct and transmitted power of a laser beam in an auxiliary experiment. According to [20, 44–47], the output power P_{out} is given by

$$P_{\text{out}} = P_{\text{sat}} \mathcal{T}_{\text{oc}} \left[\frac{G_0}{\mathcal{T}_{\text{oc}} + \mathcal{L}_{\text{par}}} - 1 \right], \quad (11)$$

where P_{sat} is the gain medium saturation power and G_0 the laser gain. We performed a nonlinear curve fit yielding $\mathcal{L}_{\text{par}} = (0.0101 \pm 0.0006)$, $P_{\text{sat}} = (26.3 \pm 2.0) \text{ W}$ and $G_0 = (0.150 \pm 0.006)$. The measured losses \mathcal{L}_{par} of $\sim 1\%$ are in accordance with expectations for a cavity made of four mirrors (three high reflection mirrors plus the output mirror), three AR-coated crystals and a Brewster plate. In Annex A we relate the values measured for P_{sat} and G_0 to the parameters of the lasing crystal and the laser cavity. We find good agreement with literature values.

6.2 Doubling and frequency behavior

Several Nd:YVO_4 lasers emitting at 671 nm have been built based on intra-cavity frequency doubling using a LBO (lithium triborate, LiB_3O_5) crystal [6–14]. The largest achieved power was 5.5 W but none of these lasers have run in SLM operation. We have tried frequency doubling with both LBO and BIBO (bismuth triborate, BiB_3O_6) crystals installed in the small waist of the laser cavity (see Fig. 1). The BIBO crystal gave slightly more power but with a substantially more astigmatic laser mode. Therefore we use a LBO crystal of 15 mm length and $3 \times 3 \text{ mm}^2$ cross-section. We apply type I SH generation, with critical phase matching at

$\theta = 86.1^\circ$ and $\phi = 0^\circ$. The crystal is AR coated with a specified residual reflection equal to 0.15% at 1342 nm and 0.5% at 671 nm.

The non-linear optical coefficient of LBO is $d_{\text{eff}} = 0.817 \text{ pm.V}^{-1}$. Using the expressions given in ref. [48] and the SNLO software [49] to evaluate the crystal properties, we have calculated the expected optimum conversion coefficient η for this crystal.

We get $\eta = 7.3 \times 10^{-5} \text{ W}^{-1}$ with an optimum waist in the crystal equal to $w_0 = 29 \mu\text{m}$. We use a slightly larger laser waist of $\simeq 45 \mu\text{m}$ for which theory predicts $\eta = 4.9 \times 10^{-5} \text{ W}^{-1}$. We have measured η by running the laser with a weakly IR-transmitting mirror M_2 , with a coupling transmission value $\mathcal{T}_{\text{oc}} = (0.55 \pm 0.03)\%$, and by measuring simultaneously the emitted power at both 1342 nm and 671 nm. We have found $\eta = (4.7 \pm 0.5) \times 10^{-5} \text{ W}^{-1}$, in excellent agreement with the theoretical value.

Finally by replacing the IR-transmitting mirror M_2 by a highly reflective one, we have extracted the SH output through mirror M_3 which has a transmission near 95% at 671 nm. When the laser operates at the peak of its gain curve, corresponding to a visible emission near 671.1 nm, we get up to 1 W of SH light. At the lithium resonance wavelength 670.8 nm and with an intra-cavity 500- μm -thick etalon made of fused silica and with a reflectivity of $\mathcal{R} \simeq 30\%$, the current output power reaches $\sim 600 \text{ mW}$. Progress towards frequency-stabilization as described in Section 4.2 is ongoing. With this simpler optical system we expect performances comparable to those obtained with external cavity frequency doubling presented in Section 3.3.

7 Conclusion

We have presented a frequency-stabilized laser source to address the D-line transitions in atomic lithium. Up to 670 mW single mode output power has been generated, currently limited by intensity-dependent effects in the doubling crystal. Tunability, narrow-band spectral quality and stable long-term locked operation were demonstrated. This proves the suitability of the system as a laser source for experiments involving cooling and trapping of lithium species. We also presented first results of a simpler alternative setup featuring intra-cavity doubling. Higher output powers could be achieved by optimizing the doubling cavity design for less intensity in the ppKTP crystal by enlarging the waist or using less thermally sensitive doubling nonlinear materials. Further increase of the laser power at 1342 nm is feasible using a pump source at 888 nm [24], reducing the quantum defect and thus the detrimental thermal effects.

Acknowledgements We would like to thank Y. Louyer, P. Juncar and F. Balembois for their help in starting this development, J.L. Doualan, R. Moncorg and P. Camy for a new measurement of the stimulated cross section of Nd:YVO₄, E. Mimoun for providing his design of the lock circuitry, N. Navon for his help in conducting the linewidth measurements, F. Lenhardt, P. Zimmermann and J.J. Zondy for fruitful discussions and R. Stein and A. Grier for careful reading of the manuscript. The LKB team acknowledges financial support from ERC (FerLoDim project), EuroQUAM (FerMix), IFRAF, IUF, ESF, ANR, SCALA and DARPA (OLE project) and the LCAR team acknowledges financial support from CNRS INP, BNM (grant 04-3-004), ANR (grant ANR-05-BLAN-0094) and Région Midi-Pyrénées.

A Additional materials

The theoretical values of P_{sat} and G_0 are given by

$$G_0 = \eta_Q \eta_0 \frac{\lambda_p}{\lambda_l} \times \frac{P_{\text{abs}}}{P_{\text{sat}}}, \quad (12)$$

$$P_{\text{sat}} = \eta_0 I_{\text{sat}} \frac{V_{\text{eff}}}{L_{\text{med}}}, \quad (13)$$

where η_0 is the overlap efficiency of the pump and laser cavity mode in the gain medium, η_Q the quantum efficiency of emission, V_{eff} the gain medium effective volume and L_{med} its length, λ_p and λ_l the pump and laser wavelength respectively and P_p the pump laser power. In [20, 44–47] the length L_{med} is multiplied by 2 because the calculation concerns standing-wave cavities and this factor is suppressed in the case of a ring cavity. Ref. [46] gives the general expressions of $V_{\text{eff}}/L_{\text{med}}$ and of η_0 as a function of the laser mode waist w_1 and pump mode waist w_p .

In our experiment, the pump mode is obtained by expanding the mode emitted by a 200- μm diameter optical fiber of $NA = 0.22$ by a factor of 5. After expansion, the pump mode divergence is small and it is a reasonably good approximation to assume that the pump mode waist is constant over the crystal volume. We get

$$\eta_0 = \frac{w_1^2 (w_1^2 + 2w_p^2)}{(w_1^2 + w_p^2)^2} = 0.63, \quad (14)$$

$$\frac{V_{\text{eff}}}{L_{\text{med}}} = \frac{\pi}{2} (w_1^2 + 2w_p^2) = 6.4 \times 10^{-3} \text{ cm}^2, \quad (15)$$

where we have used for the laser mode waist the value $w_1 = 400 \mu\text{m}$ calculated at the position of the Nd:YVO₄ crystal. This calculation assumes that the thermal focal length of this crystal is 100 mm but the mode parameters are not very sensitive to this focal length, because its position is close to the large waist of the laser cavity. The pump mode waist $w_p = 500 \mu\text{m}$ is deduced from the fiber diameter and the expansion ratio.

By combining G_0 and P_{sat} , we get $\eta_0 = 0.50 \pm 0.06$, reasonably close to our theoretical value. To get the value of $V_{\text{eff}}/L_{\text{med}}$, we need to know the saturation intensity $I_{\text{sat}} = h\nu_1/\sigma\tau_e$ where σ is the stimulated emission cross-section, τ_e the excited state lifetime and $\nu_1 = c/\lambda_1$. The maximum value of σ for stimulated emission near $\lambda_1 = 1342 \text{ nm}$ is $\sigma = 17 \times 10^{-20} \text{ cm}^2$: this value was measured with a spectral resolution near 2.5 nm [50] and the same value has been

found in an unpublished study [18]. The excited state lifetime increases when the Neodymium ion concentration decreases [19, 51]. We have used the largest literature value $\tau_e = 1.1 \times 10^{-4}$ s corresponding to a 0.4% Nd concentration. We thus get $I_{\text{sat}} = 7.9 \pm 0.8$ kW/cm², with an estimated 10% error bar. The quantum yield η_Q depends on the Neodymium ion concentration [52] and practically $\eta_Q = 1$ for 0.2 at.%-doped crystals. By combining our measured values of G_0 and P_{sat} , we deduce $V_{\text{eff}}/L_{\text{med}} = (6.6 \pm 0.9) \times 10^{-3}$ cm² in good agreement with eq. (15). This gives confidence in our determination of the 1% loss of our cavity without second harmonic generation.

References

1. C. Chin, R. Grimm, P. Julienne, and E. Tiesinga, *Rev. Mod. Phys.* **82**, 1225 (2010).
2. J. T. F. Johnston, R. H. Brady, and W. Proffitt, *Appl. Opt.* **21**, 2307 (1982).
3. A. Miffre, M. Jacquey, M. Büchner, G. Tréneç, and J. Vigué, *Physica Scripta* **74**, C15 (2006).
4. S. A. Payne, L. K. Smith, R. J. Beach, B. H. T. Chai, J. H. Tassano, L. D. DeLoach, W. L. Kway, R. W. Solarz, and W. F. Krupke, *Appl. Opt.* **33**, 5526 (1994).
5. I. E. Olivares, A. E. Duarte, E. A. Saravia, and F. J. Duarte, *Appl. Opt.* **41**, 2973 (2002).
6. A. Agnesi, A. Guandalini, and G. Reali, *J. Opt. Soc. Am. B* **19**, 1078 (2002).
7. A. Agnesi, A. Guandalini, G. Reali, S. Dell'Acqua, and G. Piccinno, *Opt. Lett.* **29**, 56 (2004).
8. Y.-F. L, X.-H. Zhang, J. Xia, X.-D. Yin, A.-F. Zhang, L. Bao, and W. L, *Optics & Laser Technology* **42**, 522 (2010).
9. H. Ogilvy, M. Withford, P. Dekker, and J. Piper, *Opt. Express* **11**, 2411 (2003).
10. A.-Y. Yao, W. Hou, X.-C. Lin, Y. Bi, R.-N. Li, D.-F. Cui, and Z.-Y. Xu, *Optics Communications* **231**, 413 (2004).
11. A.-Y. Yao, W. Hou, Y. Bi, A.-C. geng, X.-C. Lin, Y.-P. Kong, D.-F. Cui, L.-A. Wu, and Z.-Y. Xu, *Appl. Opt.* **44**, 7156 (2005).
12. L. Zhang, C. Li, D. Li, P. Li, Q. Zhang, and Z. Zhang, *Optics & Laser Technology* **37**, 524 (2005).
13. Q. Zheng, H. Tan, L. Zhao, and L. Qian, *Optics & Laser Technology* **34**, 329 (2002).
14. Q. Zheng, J.-Y. Wang, and L. Zhao, *Optics & Laser Technology* **36**, 485 (2004).
15. F. Lenhardt, A. Nebel, R. Knappe, M. Nittmann, J. Bartschke, and J. A. L'huillier, in *Conference on Lasers and Electro-Optics* (Optical Society of America, San Jose, CA, USA, 2010), p. CThEE5.
16. R. Sarrouf, V. Sousa, T. Badr, G. Xu, and J.-J. Zondy, *Opt. Lett.* **32**, 2732 (2007).
17. A. E. Siegman, *Lasers* (University Science Books, Mill Valley, California, 1986).
18. J. Doualan, P. Camy, and R. Moncorgé, private communication (unpublished).
19. M. Okida, M. Itoh, T. Yatagai, H. Ogilvy, J. Piper, and T. Omatsu, *Opt. Express* **13**, 4909 (2005).
20. Y. F. Chen, T. M. Huang, C. F. Kao, C. L. Wang, and S. C. Wang, *IEEE Journal of Quantum Electronics* **33**, 1424 (1997).
21. G. Tréneç, W. Volondat, J. Vigué, and O. Cugat, in preparation (unpublished).
22. R. Sarrouf, T. Badr, and J. J. Zondy, *Journal of Optics A: Pure and Applied Optics* **10**, 104011 (2008).
23. W. Leeb, *Applied Physics A: Materials Science & Processing* **6**, 267 (1975), 10.1007/BF00883762.
24. L. McDonagh, R. Wallenstein, R. Knappe, and A. Nebel, *Opt. Lett.* **31**, 3297 (2006).
25. F. Song, C. Zhang, X. Ding, J. Xu, G. Zhang, M. Leigh, and N. Peyghambarian, *Applied Physics Letters* **81**, 2145 (2002).
26. D. B. Leviton, B. J. Frey, and T. J. Madison, *Proc. SPIE* 6692, 669204 (2007).
27. G. D. Boyd and D. A. Kleinman, *Journal of Applied Physics* **39**, 3597 (1968).
28. L. E. Myers, R. C. Eckardt, M. M. Fejer, R. L. Byer, W. R. Bosenberg, and J. W. Pierce, *J. Opt. Soc. Am. B* **12**, 2102 (1995).
29. R. Boyd, *Nonlinear Optics* (Academic Press, San Diego, 2003).
30. M. Peltz, U. Bäder, A. Borsutzky, R. Wallenstein, J. Hellström, H. Karlsson, V. Pasiskevicius, and F. Laurell, *Applied Physics B: Lasers and Optics* **73**, 663 (2001), 10.1007/s003400100733.
31. C. Canalas, S. Wang, V. Pasiskevicius, and F. Laurell, *Applied Physics Letters* **88**, 032905 (2006).
32. K. Fradkin, A. Arie, A. Skliar, and G. Rosenman, *Applied Physics Letters* **74**, 914 (1999).
33. S. Emanuelli and A. Arie, *Appl. Opt.* **42**, 6661 (2003).
34. E. Mimoun, L. D. Sarlo, J.-J. Zondy, J. Dalibard, and F. Gerbier, *Opt. Express* **16**, 18684 (2008).
35. V. A. Maslov, V. A. Mikhailov, O. P. Shaunin, and I. A. Shcherbakov, *Quantum Electronics* **27**, 356 (1997).
36. B. Boulanger, I. Rousseau, J. P. Feve, M. Maglione, B. Menaert, and G. Marnier, *IEEE Journal of Quantum Electronics* **35**, 281 (1999).
37. F. Torabi-Goudarzi and E. Riis, *Optics Communications* **227**, 389 (2003).
38. A. Arie, G. Rosenman, A. Korenfeld, A. Skliar, M. Oron, M. Katz, and D. Eger, *Opt. Lett.* **23**, 28 (1998).
39. E. Mimoun, L. De Sarlo, J.-J. Zondy, J. Dalibard, and F. Gerbier, *Applied Physics B: Lasers and Optics* **99**, 31 (2010), 10.1007/s00340-009-3844-x.
40. S. Nascimbène, N. Navon, K. J. Jiang, L. Tarruell, M. Teichmann, J. McKeever, F. Chevy, and C. Salomon, *Phys. Rev. Lett.* **103**, 170402 (2009).
41. W. I. McAlexander, E. R. I. Abraham, and R. G. Hulet, *Phys. Rev. A* **54**, R5 (1996).
42. F. Biraben, *Optics Communications* **29**, 353 (1979).
43. R. Smith, *IEEE Journal of Quantum Electronics* **6**, 215 (1970).
44. W. W. Rigrod, *Journal of Applied Physics* **36**, 2487 (1965).
45. P. Laporta and M. Brussard, *IEEE Journal of Quantum Electronics* **27**, 2319 (1991).
46. Y. F. Chen, T. S. Liao, C. F. Kao, T. M. Huang, K. H. Lin, and S. C. Wang, *IEEE Journal of Quantum Electronics* **32**, 2010 (1996).
47. Y. F. Chen, L. J. Lee, T. M. Huang, and C. L. Wang, *Optics Communications* **163**, 198 (1999).
48. F. J. Kontur, I. Dajani, Y. Lu, and R. J. Knize, *Opt. Express* **15**, 12882 (2007).
49. SNLO software, <http://www.as-photonics.com/SNLO.html>.
50. L. Fornasiero, S. Kück, T. Jensen, G. Huber, and B. Chai, *Applied Physics B: Lasers and Optics* **67**, 549 (1998), 10.1007/s003400050543.
51. A. W. Tucker, M. Birnbaum, C. L. Fincher, and J. W. Erler, *Journal of Applied Physics* **48**, 4907 (1977).

52. Y.-F. Chen, IEEE Journal of Quantum Electronics **35**, 234 (1999).